



Mechanisms of mechanochemical synthesis of cesium lead halides: pathways toward stabilization of $\alpha\text{-CsPbI}_3$

Eduard Aleksanyan^{1,*}, Ani Aprahamian², Alexander S. Mukasyan³, Vachagan Harutyunyan¹, and Khachatur V. Manukyan^{2,*}

¹ Applied Physics Researches Division, A. Alikhanyan National Laboratory (Yerevan Physics Institute), 0036 Yerevan, Armenia

² Nuclear Science Laboratory, Department of Physics, University of Notre Dame, Notre Dame, IN 46556, USA

³ Department of Chemical and Biomolecular Engineering, University of Notre Dame, Notre Dame, IN 46556, USA

Received: 24 December 2019

Accepted: 27 March 2020

Published online:

8 April 2020

© Springer Science+Business Media, LLC, part of Springer Nature 2020

ABSTRACT

Cesium lead iodide with cubic perovskite structure ($\alpha\text{-CsPbI}_3$) is gaining significant interest in photovoltaic applications due to its excellent absorbance of the visible solar light and other attractive optoelectronic properties. However, the synthesis of stable $\alpha\text{-CsPbI}_3$ poses a significant challenge. Mechanochemical synthesis is emerging as a suitable method for the preparation of cesium lead halides. This work investigates the ball milling-induced synthesis of cesium lead halides perovskite phase using halide mixing or doping approaches. The synthesis in the $\text{CsI} + \text{PbI}_2$, $\text{CsBr} + \text{PbBr}_2$, $\text{CsBr} + \text{PbI}_2$, and $\text{CsI} + \text{PbI}_2 + \text{NdI}_3$ mixtures and halide exchange reactions in the $\text{CsPbBr}_3 + 3\text{KI}$ and $\text{CsBr} + \text{PbBr}_2 + 3\text{KI}$ systems are investigated to elucidate the mechanism of this process. Then, $\text{CsPb}(\text{I}_{1-x}\text{Br}_x)_3$ and $\text{CsPb}(\text{I}_{1-y}\text{Nd}_y)_3$ materials with different x and y ratios are prepared, and their stability is probed in the air using light absorption spectroscopy. These results suggest that Nd doping is more efficient in the stabilization of the perovskite structure than partial replacement of iodine with bromine. Microstructure observations reveal the existence of two different product formation mechanisms depending on the mechanical properties of reactants. The results reveal that the milling temperature has a significant impact on the reaction kinetics. The produced particles nucleate and grow at the reactant interface and retard the synthesis reaction by creating a diffusion barrier. Extended milling reduces the product particle size and creates fresh contact between reactants, thus facilitating reaction completion.

Address correspondence to E-mail: aeduard@yerphi.am; kmanukya@nd.edu

Introduction

Lead halide perovskites with the general formula of $APbX_3$ containing organic or inorganic monovalent cation, where A can be methylammonium, formamidinium, or cesium and the X can be halogen (Cl, Br, I) anions, have demonstrated an impressive increase in photoconversion efficiency [1–5]. Among these materials, $CsPbX_3$ are gaining significant interest due to their high absorptivity, high charge carrier mobility, defect tolerance, tunable optical property, high photoluminescence quantum yield, as well as low volatility [5–9]. These exciting properties make $CsPbX_3$ materials ideal for solar cells and solar concentrators, light-emitting devices, as well as photodetector applications [10–12].

α - $CsPbI_3$, with a bandgap of 1.73 eV, is a very suitable candidate for photovoltaic application in tandem solar cells due to its excellent absorbance of solar light [6, 7, 13, 14]. However, the synthesis of α - $CsPbI_3$ poses significant challenges, as it is stable only at high temperatures. In bulk form, α - $CsPbI_3$ transforms to other phases under different conditions [8, 11, 14]. For example, Marronnier et al. [15] and Sutton et al. [16] have demonstrated that α - $CsPbI_3$ exists only above 370 °C. At lower temperatures, it converts to the β -tetragonal and then γ -orthorhombic metastable phase. The latter transforms into the orthorhombic non-perovskite yellow δ - $CsPbI_3$ phase. The heating of the δ - $CsPbI_3$, however, results in the direct transition to the α - $CsPbI_3$ [15]. The perovskite to non-perovskite transformation is rapid when moisture is present. The underlying mechanism of moisture-assisted polymorph change is not fully understood [8]. Relatively large (100–200 nm) α - $CsPbI_3$ nanocrystals degrade into the δ - $CsPbI_3$ rapidly, while the smaller (5–15 nm) colloidal nanocrystals are relatively stable at ambient temperature due to the presence of surface capping agents or organic solvent environment [17].

A general strategy to enhance the phase stability of cubic α - $CsPbI_3$ involves the modulations (doping, alloying, or mixing) of A, B, and X sites by tuning the Goldschmidt tolerance ($\tau = \frac{r_A+r_X}{\sqrt{2}(r_B+r_X)}$) and octahedral ($\mu = \frac{r_B}{r_X}$) factors, where r_A and r_B are the radii of Cs and Pb cations and r_X is the radius of halogen anion [14, 18]. As a rule of thumb, the cubic

perovskite phase is stable if τ and μ are higher than 0.875 and 0.41, respectively [18]. Another work suggests that the τ value between 0.8 and 1.0 is more favorable for the cubic perovskite structure stability [19]. The values of these factors for α - $CsPbI_3$ ($\tau = 0.81$ –0.89 and $\mu = 0.47$) are close to the above limits, thus making it a metastable material [14, 19]. The B-site (Pb) modulation significantly influences both τ and μ values. Many iconic species (such as Mn^{2+} , Sr^{2+} , Sn^{2+}) are capable of substituting Pb. Incorporation of Mn^{2+} enables significant stabilization of nanoscale α - $CsPbI_3$ without modification of the bandgap energy [20, 21]. Doping or alloying with Sr^{2+} or Sn^{2+} shows stabilization of the perovskite structure, but also changes the bandgap energies of resulting materials [22, 23]. Several trivalent ions (Bi^{3+} , Sb^{3+} , Eu^{3+}) are also reported to replace the Pb sites [24–26]. That changes the charge neutrality and influences the optical properties. The X-site modulation (halide mixing) is explored [27–29] more broadly. Partial replacement of I with Cl or Br significantly enhances the stability of nanoscale perovskite systems by tuning the octahedral factor. This modification also allows fine-tuning of the bandgap energy of resulting mixed perovskites.

The primary synthesis method for most lead halide perovskites is based on solution processing of halide salts dissolved in dimethylformamide or dimethyl sulfoxide, followed by the deposition of thin films by spin coating [1, 4, 5, 12, 14, 20, 22, 24, 26]. Even though this method has proven to form excellent materials, there are several drawbacks which include the limited choice of solvents, the toxicity of some of the solvents, a limited possibility for upscaling, and difficulty in controlling the composition and stoichiometry. Recently, mechanochemical synthesis has emerged as a suitable solvent-free method for the preparation of lead halide perovskites [2, 30–33]. The process is simple and can be performed even by manual grinding of the halides using a mortar and a pestle [31, 32, 34–40]. This approach is especially useful in the preparation of complex perovskites [34, 40–43], which are difficult to produce by the solution processing methods due to the limited choice of suitable solvents capable of dissolving the multiple reactants [32, 44–46]. The mechanochemical synthesis also provides versatile pathways for modulation of B- or X-sites in perovskites [31, 38, 40, 45, 47–50]. The use of mechanical ball mills

also permits large-scale synthesis of these materials [30, 34, 51].

The mechanistic aspects of the process, however, remain mostly unknown. There are only a few works reported on attempts at ball milling-induced structural and morphological transformations which take place during the synthesis. For example, in the $\text{CH}_3\text{NH}_3\text{I} + \text{PbI}_2$ system, the product ($\text{CH}_3\text{NH}_3\text{PbI}_3$) forms gradually without any intermediate compounds during the milling [30, 52]. The milling in all-inorganic $\text{CsBr} + \text{PbBr}_2$ mixture forms CsPbBr_3 , CsPb_2Br_5 , and Cs_4PbBr_6 at the early stages [53]. Then, further milling results in the transition of non-stoichiometric compounds to the CsPbBr_3 phase. These results suggest that more works should be conducted to increase our understanding of the mechanisms that govern the reaction, as well as structural and morphological refinements taking place during milling. Furthermore, the factors that influence the uniformity of small amounts of dopants during their in situ incorporation into the perovskite matrix are also unknown.

This work aims to investigate the preparation of stable cesium lead halides perovskites under the mechanochemical synthesis conditions using either B- or X-site modulations. To understand the mechanism of the reactions in the $\text{CsI} + \text{PbI}_2$, $\text{CsBr} + \text{PbBr}_2$, $\text{CsBr} + \text{PbI}_2$ and $\text{CsI} + \text{PbI}_2 + \text{NdI}_3$ systems and halide exchange reactions in the $\text{CsPbBr}_3 + 3\text{KI}$ and $\text{CsBr} + \text{PbBr}_2 + 3\text{KI}$ are investigated under different conditions. Then, $\text{CsPb}(\text{I}_{1-x}\text{Br}_x)_3$ and $\text{CsPb}(\text{I}_{1-y}\text{Nd}_y)_3$ materials preparation is studied depending on the x and y ratios. The stability of the CsPbI_2Br and $\text{CsPb}_{0.9}\text{Nd}_{0.1}\text{I}_3$ material is probed using absorption spectroscopy. A general mechanism of mechanochemical reactions and their relations to stabilization of the perovskite phases are discussed.

Materials and methods

Cesium iodide (CsI , 99.9%, BeanTown Chemicals), lead iodide (PbI_2 , 99.9985, Alfa Aesar), cesium bromide (CsBr , 99.999%, Aldrich), lead bromide (PbBr_2 , 99.999%, Aldrich), potassium iodide (KI , 99.9%, Alfa Aesar), and neodymium iodide (NdI_3 , 99.9%, Aldrich) were used as reactants for mechanochemical synthesis without further purification. The desired quantities of reactants were measured inside a glove box filled with inert gas and then transferred into

stainless steel (25 ml volume) jar, followed by adding stainless steel balls (with 10 mm diameter). The ball-to-powder ratio in all experiments was 15:1. Ball milling was conducted in CryoMill (Retsch) with or without liquid nitrogen cooling at 30 Hz shaking frequency. The milling time was varied from 5 to 180 min. After treatment, the milling jar was opened in a glove box, and the products were collected and stored in a dry inert gas atmosphere.

Differential scanning calorimeter (DSC) from Mettler Toledo was used to determine phase transition in reactants and investigate the reactions between them in heating conditions. In these experiments, mixtures of reactants were prepared by manual mixing. Then, the mixtures were transferred into Al crucibles and sealed under an inert atmosphere. DSC experiments were performed in the 25–380 °C temperature range with a 40 °C/min heating rate.

The phase composition of materials in ambient conditions was determined by powder X-ray diffraction (XRD) analysis with Ni-filtered $\text{CuK}\alpha$ radiation using the D8-Advance (Bruker) diffractometer operated at 40 kV and 40 mA. XRD patterns of samples were measured at ambient conditions in the $2\theta = 10^\circ$ – 50° angular range with a step size of 0.01°. In some cases, a small quantity of material was inserted into Pyrex capillary tubes (200 μm inner diameter with a wall thickness of 50 μm) and sealed under an inert atmosphere. XRD patterns of these samples were obtained by rotating the capillary tubes. The morphology of the products was investigated with a field emission scanning electron microscope (Magellan 400) equipped with secondary and backscattering electron detectors and energy-dispersive X-ray spectrometer (EDS, Bruker).

Absorption measurements of the synthesized materials were conducted in the ultraviolet–visible near-infrared (UV–Vis–NIR) range (800–300 nm) using the Jasco V-670 double-beam spectrophotometer. A Jasco ISN 723 integrating sphere attachment was used, where the samples were illuminated under a small angle. The light from the sample is collected and directed to the detector (diffuse reflectance spectra). Baseline measurements allowed the determination of the absorbance of the various samples. The 850-nm grating and 1000 nm/min scan rate were used in all measurements.

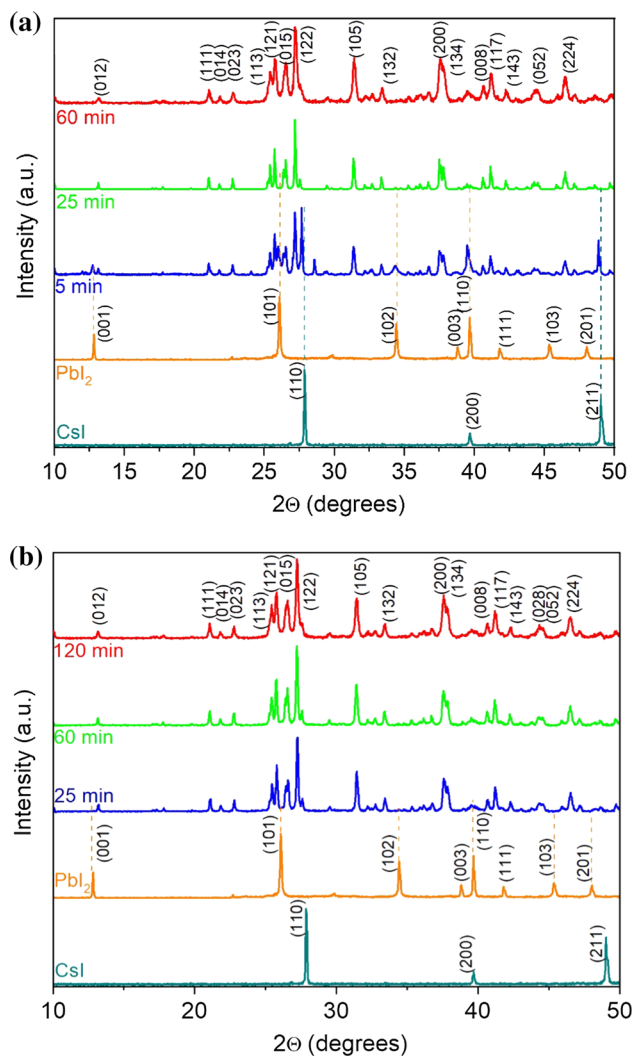


Figure 1 XRD patterns of reactants and products prepared at different milling times at cryogenic (a) and room (b) temperatures.

Results

Mechanochemical synthesis in the CsI + PbI₂ system

Figure 1 shows XRD patterns of materials prepared at different milling times in cryogenic (Fig. 1a) and room (Fig. 1b) temperatures for the CsI + PbI₂ mixture along with patterns of the initial reactants. The sample that was milled for 5 min at cryogenic temperature shows peaks for both reactants and the orthorhombic δ -CsPbI₃ phase. The peaks for reactants are broader compared to the non-milled CsI and PbI₂ powders and shifted toward the lower angular range by 0.15° – 0.25° , indicating significant lattice distortions. The XRD pattern of the sample milled for

25 min in cryogenic temperature shows intense δ -CsPbI₃ peaks together with some weak lines for reactants. After 60 min of milling, the lines for δ -CsPbI₃ become broader, while no peaks for reactant can be detected.

The sample milled for 25 min (room temperature) contains primarily δ -CsPbI₃ with insignificant quantities of reactants (Fig. 1b). There is little difference between XRD patterns of samples milled for 25 and 60 min, and the peaks for reactants are hard to detect. Prolonged milling (120 min) results in the broadening of peaks for δ -CsPbI₃. For example, a closer look at the (122) peak (see Supplementary information, Figure S1) indicates a broader full width half maximum compared to the same peak of the sample with 60 min of milling (Figure S1). This broadening can be related to the decrease in particle sizes and/or lattice strains due to extended mechanical treatment.

The precise evaluation of reactants' conversion during mechanochemical synthesis using XRD is challenging due to the significant peak broadening caused by intense lattice distortions. Therefore, we also used UV–Vis absorption spectroscopy to follow the dynamics of reactant conversion more accurately. Figure 2 shows the absorption spectra of samples prepared at different milling times and temperatures in conjunction with initial reactants. The UV–Vis spectra of reactants indicate absorption edges at ~ 400 – 450 nm and ~ 530 nm for CsI and PbI₂, respectively. The spectra of samples milled for five min in cryogenic temperature contain two absorption bands with onsets at ~ 530 nm and ~ 450 nm (Fig. 2a). The band at ~ 530 nm is related to initial PbI₂, while the one at ~ 450 nm can be attributed to the yellow δ -CsPbI₃ phase [54]. The increase in milling time from 25 to 60 min causes a decrease in the PbI₂ absorbance band. Although the XRD analysis of the sample milled for 60 min (Fig. 1a) shows only the δ -CsPbI₃ phase, the UV–Vis spectrum exhibits a weak shoulder associated with PbI₂ absorption, suggesting the incomplete conversion of reactants. The absorption band for PbI₂ disappears in samples milled at room temperature with longer milling times, such as 60 min (Fig. 2b).

Figure 3 summarizes the results of the morphological investigation of the reactants and selected milled samples. A typical CsI particle has an irregular shape with a size of ~ 150 μm . The PbI₂ particles are relatively smaller (10–30 μm), but they also have irregular shapes. SEM images of separately milled

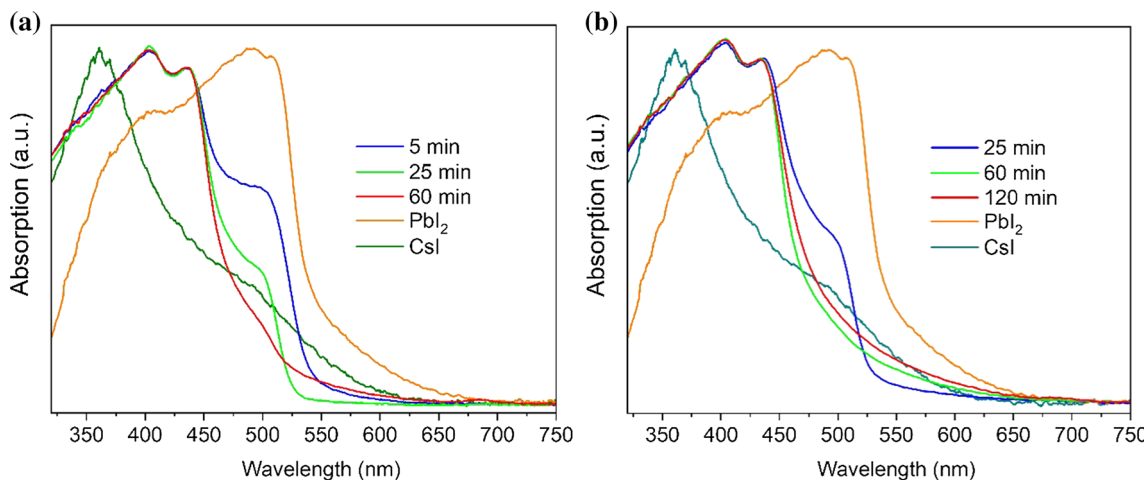


Figure 2 UV-Vis absorption of reactants and products as a function of milling times at cryogenic (a) and room (b) temperatures.

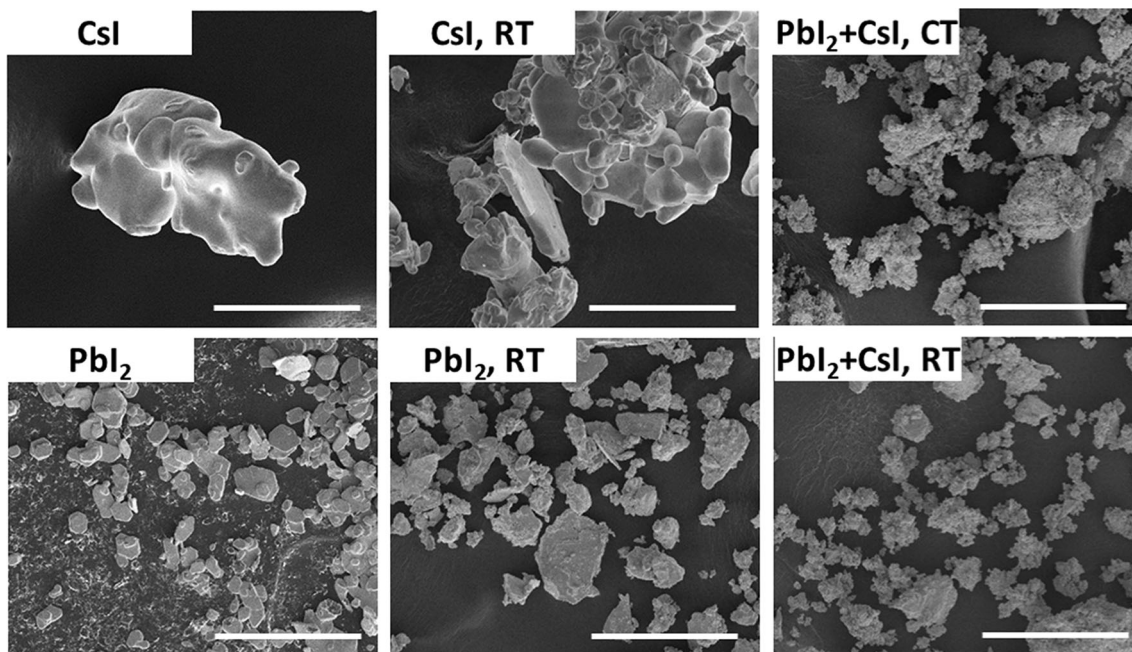


Figure 3 SEM images of CsI and PbI₂, ball-milled pure reactants and their mixtures at cryogenic (CT) and room (RT) temperatures (25-min milling). The scale bar is 100 μ m.

(with 25 min) reactants at room temperature exhibit few notable features. Although a significant portion of CsI of particles fragmented into smaller pieces (5–30 μ m), some CsI particles deformed under the dynamic collisions of the balls, resulting in thin (\sim 5 μ m) plates. Most of the PbI₂ particles plastically deformed to form flat disks. The CsI + PbI₂ mixture that was milled both at cryogenic and room temperatures for 25 min exhibits relatively small aggregates.

A closer look at the morphology of the products reveals the effect of temperature and milling time on

δ -CsPbI₃ particles (Fig. 4). SEM images show that the majority of product particles produced at cryomilling conditions exhibit near-spherical shapes except for a few particles with faceted (cubic) shape and brighter contrast. Based on the absorption measurements presented in Fig. 2a, we can suggest that these particles can be the non-reacted precursors. The average size of the individual crystallites in the agglomerates of the cryomilled sample for 5 min is \sim 200 nm. Further milling to 25 min results in a small increase

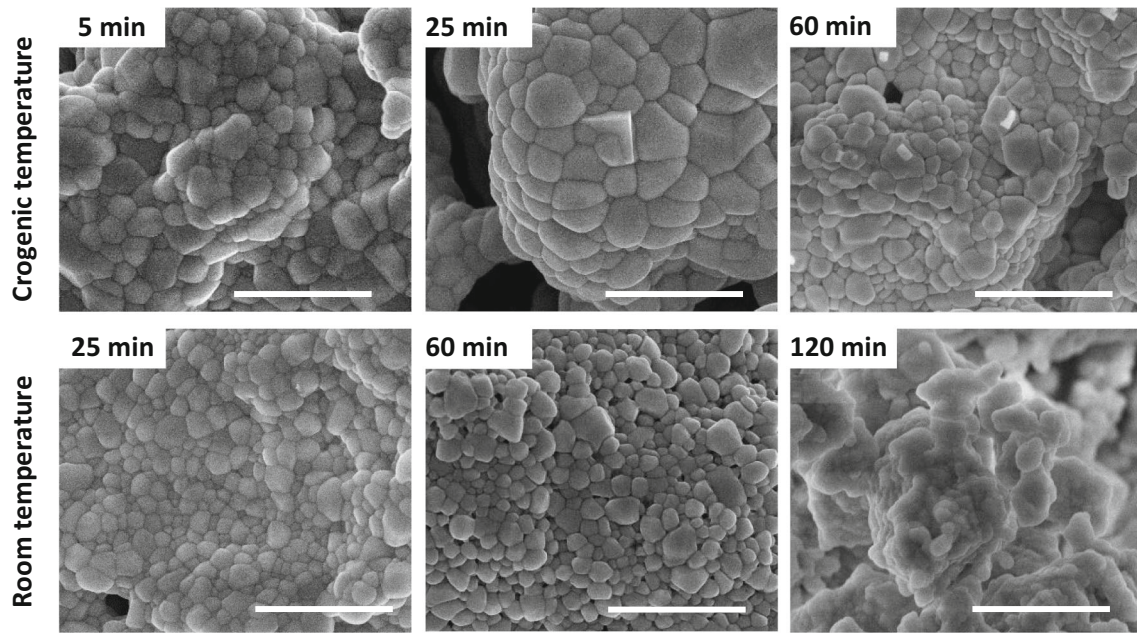


Figure 4 SEM images of δ -CsPbI₃ products prepared at different milling times and temperatures. The scale bar is 1 μ m.

in particle sizes. The sample with a longer milling time (60 min) shows some particle size reduction.

A sample milled at room temperature (25 min) exhibits similar near-spherical particles with an average size of \sim 150 nm (Fig. 4). Further milling to 60 min has little influence on the size of δ -CsPbI₃ particles, while prolonged milling with 120 min results in significant distortion as well as some cold welding of particles.

The result presented in this section indicates that the temperature influences the reaction kinetics of the CsI + PbI₂ system. At cryogenic conditions, the reaction processed slower than at room temperature. XRD analysis and UV–Vis absorption measurements suggest that initial reactants gradually transform to δ -CsPbI₃ without the formation of any intermediate products. The process temperature has little effect on the δ -CsPbI₃ particle sizes.

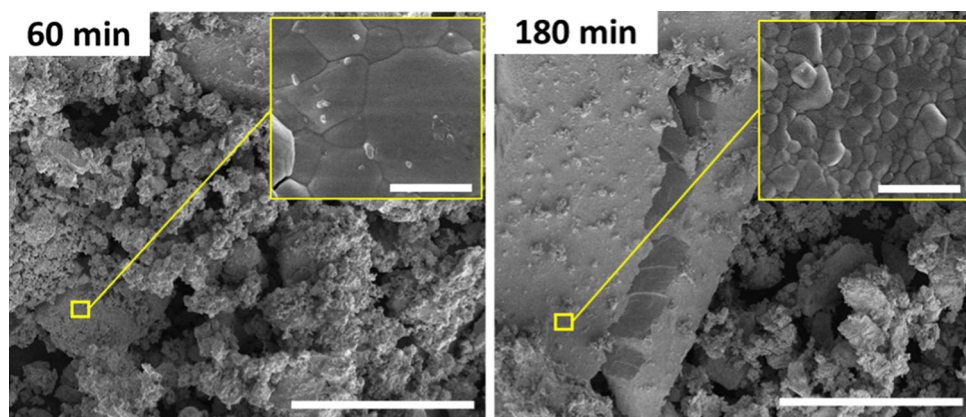
Mechanochemical synthesis in the CsBr + PbBr₂ system

The initial stages of the mechanochemical synthesis of CsPbBr₃ were investigated earlier [53]. Two intermediate compounds, CsPb₂Br₅ and Cs₄PbBr₆, were identified during the first 5 min of milling. In this work, we study the ball milling in the stoichiometric CsBr + PbBr₂ mixture at longer milling times. Figure S2 shows XRD patterns for the samples prepared

at 60- and 180-min milling times at room temperature along with XRD patterns of reactants. These results indicate that reactants fully converted into the pure orthorhombic CsPbBr₃ (orange-color) phase for both milling times. The product prepared at 60 min of milling exhibits relatively sharp and well-resolved diffraction peaks. Prolonged milling leads to some broadening of peaks.

Figure 5 presents the microstructures of CsPbBr₃ powders, while SEM images of CsBr and PbBr₂ are shown in Figure S3. Both reactants consist of coarse (100–300 μ m) irregular particles. The low-magnification image of 60-min milled sample shows porous particle agglomerates (Fig. 5). The higher-magnification image shown as an inset in Fig. 5 displays that the particle sizes of CsPbBr₃ vary between 200 and 2000 nm. Further mechanical treatment (180 min) leads to the formation of large (hundreds of micrometers) densely packed but brittle agglomerates (Fig. 5). We can assume that such agglomerates may form by a cold-welding process similar to reported in all metallic and metal–non-metal systems [55, 56]. The size of individual particles, however, is smaller (200–500 nm), as shown by an SEM image inset presented in Fig. 5. Thus, prolonged milling allows decreasing the sizes of individual CsPbBr₃ particles, but simultaneously increases the agglomerate size by enhancing the cold welding. UV–Vis measurements of CsPbBr₃ products prepared at

Figure 5 SEM images of CsPbBr_3 prepared at different milling times. The scale bars are 100 and 1 μm in the large panels and insets, respectively.



60 min of milling show a sharp absorption edge at 550 nm wavelength (Figure S4), indicating the full conversion of the reactants into the desired product.

Mechanochemical synthesis in the $\text{CsBr} + \text{PbBr}_2 + 3\text{KI}$ and $\text{CsPbBr}_3 + 3\text{KI}$ systems

We also investigate the mechanochemical reaction in the $\text{CsPbBr}_3 + 3\text{KI}$ and $\text{CsBr} + \text{PbBr}_2 + 3\text{KI}$ mixtures. Both these samples have brown-black color after room-temperature synthesis (60-min milling time). The dark color of the samples suggests that such halide exchange offers some potential to prepare materials with perovskite structure that could absorb visible solar light.

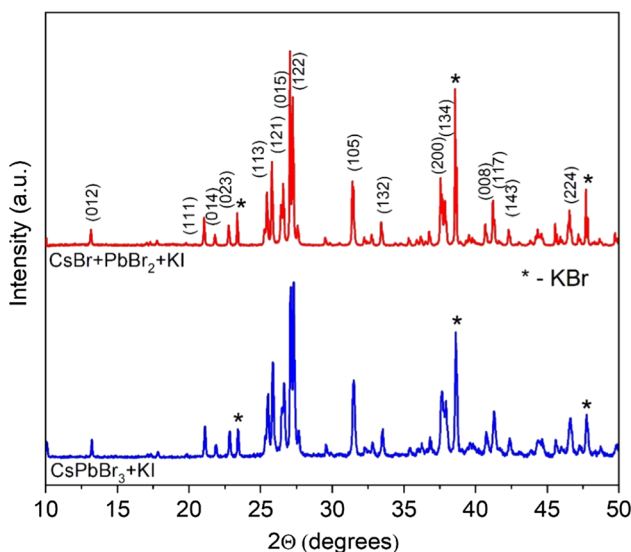


Figure 6 XRD patterns of $\delta\text{-CsPbBr}_3$ prepared by room-temperature milling of the $\text{CsPbBr}_3 + 3\text{KI}$ and $\text{CsBr} + \text{PbBr}_2 + 3\text{KI}$ mixtures for 60 min.

The color of both samples, however, turns to the yellow quickly, and products show a similar phase composition of $\delta\text{-CsPbI}_3$ and KBr (Fig. 6). $\delta\text{-CsPbI}_3$ obtained from the $\text{CsPbBr}_3 + 3\text{KI}$ mixture has sharper diffraction peaks compared to the material prepared from the $\text{CsBr} + \text{PbBr}_2 + 3\text{KI}$ sample.

SEM images taken by a backscattering electron detector for both samples show particles with brighter contrast ($\delta\text{-CsPbBr}_3$) mixed with darker (KBr) phase (Fig. 7). The sample prepared from the $\text{CsPbBr}_3 + 3\text{KI}$ mixture exhibits coarse (Fig. 7) $\delta\text{-CsPbBr}_3$ particles (primarily in the 200–600 nm range). These $\delta\text{-CsPbBr}_3$ particles have similar sizes as the CsPbBr_3 initial material (see Fig. 5). The material prepared from the $\text{CsBr} + \text{PbBr}_2 + 3\text{KI}$ mixture exhibits narrower particle size distributions (50–300 nm) for $\delta\text{-CsPbI}_3$ (Fig. 7). These results suggest that such direct and indirect halide exchange reactions allow tailoring of the particle sizes for the products.

Stabilization of perovskite phase by modulation

The B- and X-site modulations are feasible ways to stabilize the perovskite phase. In this work, we investigate the mechanochemical synthesis of $\text{CsPb}(\text{I}_{1-x}\text{Br}_x)_3$ and $\text{CsPb}_{(1-y)}\text{Nd}_y\text{I}_3$ materials. Both types of materials obtained at room-temperature ball milling of $\text{CsI} + \text{CsBr} + \text{PbI}_2$ and $\text{CsI} + \text{PbI}_2 + \text{NdI}_3$ systems yield black powders (Figure S5), indicating the formation of the perovskite phase, which is also confirmed by XRD analysis. For example, Fig. 8 shows XRD patterns of CsPbI_2Br ($x = 0.333$) and $\text{CsPb}_{0.9}\text{Nd}_{0.1}\text{I}_3$ ($y = 0.1$) materials prepared at room temperature. Both patterns suggest the formation of

Figure 7 SEM (backscattering electron detector) images and particle size distributions of δ -CsPbBr₃ prepared at room-temperature milling of the CsPbBr₃ + 3KI and CsBr + PbBr₂ + 3KI mixtures and 60-min milling time. The scale bar is 1 μ m.

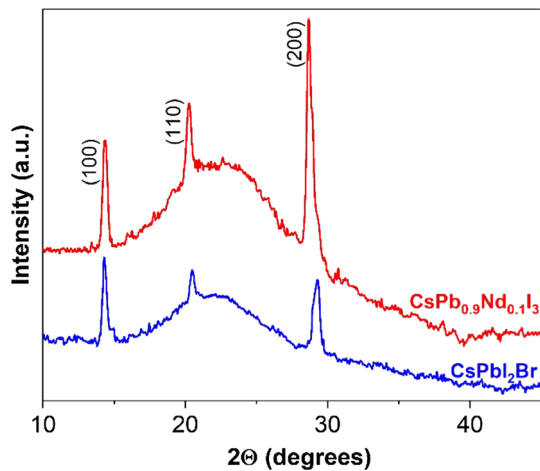
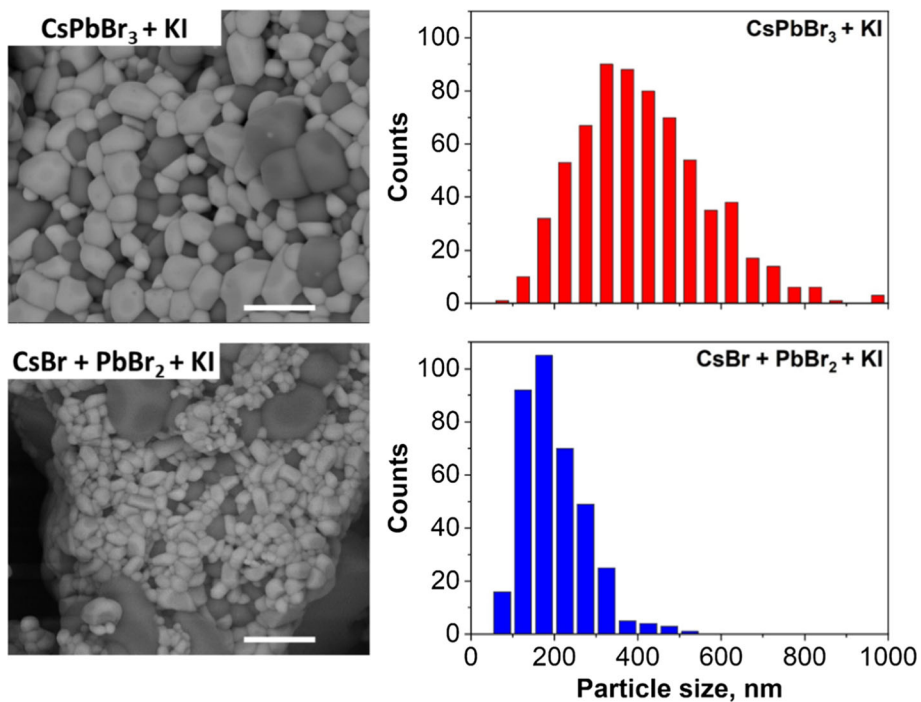


Figure 8 XRD patterns of α -CsPbBr₃ prepared by room-temperature milling of the CsPbI₂Br and CsPb_{0.9}Nd_{0.1}I₃ materials prepared at room-temperature milling for 60 min. The hump at 15°–35° range is attributed to X-ray scattering from the Pyrex glass capillary sample holder.

the cubic (black) phase confirmed by three major diffraction peaks. A broad hump at 15°–35° angular range is attributed to X-ray scattering from the Pyrex glass capillary sample holder.

SEM images show that the average particle size of the CsPb(I_{1-x}Br_x)₃ products is about 100 nm. Also, the particle size is independent of the x ratio within the $0 \leq x \leq 0.333$ range (Fig. 9). CsPb(I_{1-y})Nd_yI₃

sample, however, exhibits different morphological features. For example, the CsPb_{0.9}Nd_{0.1}I₃ sample is uniform and primarily consists of near-spherical particles with 100–150 nm sizes. The increase in the Nd content ($y = 0.2$) results in non-uniform morphology showing (Figure S6) near-spherical, faceted particles, and rod-like crystals. Figure 9 suggests that these faceted particles primarily exhibit cubic and octahedral shapes. The EDS elemental mapping indicates that iodine distribution in this sample is uniform (Fig. 10). Distribution of metals, however, is non-uniform, and excessive neodymium is observed in the areas where the content of faceted particles crystals is higher.

Meanwhile, in these areas, the amounts of Cs and Pb are significantly lower. These observations allow concluding that faceted particles are primarily neodymium iodide, while near-spherical particles are Nd-doped CsPbI₃. These results imply that Nd successfully incorporates into the crystal lattice of CsPbI₃ at relatively small Nd quantities ($y \leq 0.1$).

The black color of these CsPb(I_{1-x}Br_x)₃ ($x = 0.1$ –0.333) and CsPb(I_{1-y})Nd_yI₃ ($y = 0.1$) remains unchanged under the dry inert gas for many weeks. To learn more about the stability of samples in air, we investigated the UV–Vis absorption of the CsPbI₂Br and CsPb_{0.9}Nd_{0.1}I₃ as a function of time. The results of these investigations suggest that a freshly prepared

Figure 9 SEM images of $\text{CsPb}(\text{I}_{1-x}\text{Br}_x)_3$ and $\text{CsPb}_{(1-y)}\text{Nd}_y\text{I}_3$ materials prepared at room-temperature milling for 60 min. The scale bar is 1 μm .

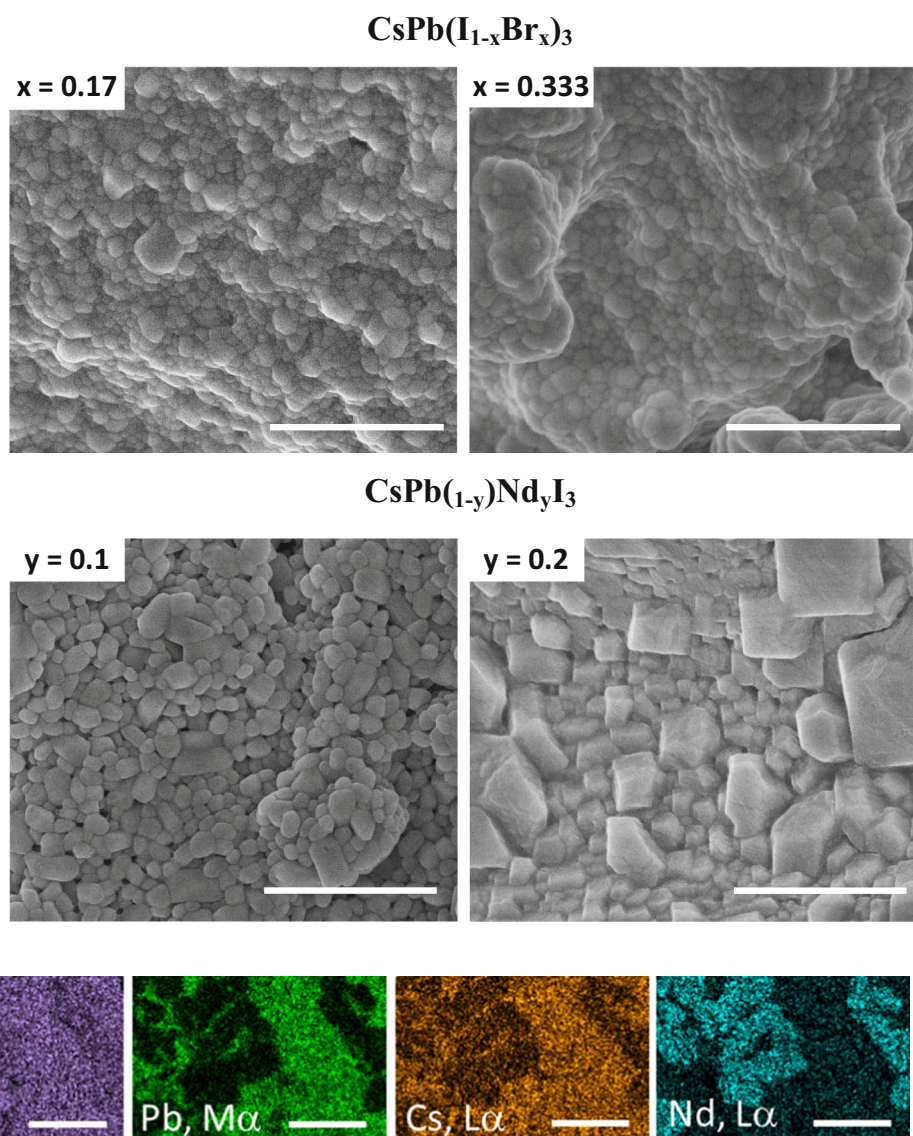


Figure 10 EDS elemental mapping of $\text{CsPb}_{0.8}\text{Nd}_{0.2}\text{I}_3$ sample prepared at room temperature and 60 min of milling. The scale bar is 20 μm .

CsPbI_2Br sample exhibits a sharp absorption edge at ~ 700 nm (Fig. 11a). UV–Vis spectra were taken during a 1–6-h period, exhibit a gradual blueshift of absorption edge to 550 nm, and the emergence of a new edge at ~ 450 nm. Further measurements up to 48 h show no significant changes.

UV–Vis spectrum of $\text{CsPb}_{0.9}\text{Nd}_{0.1}\text{I}_3$ sample exhibits an adsorption edge at ~ 720 nm and two peaks centered at ~ 750 and ~ 800 nm attributed to absorption bands of Nd^{3+} at the near-infrared region (Fig. 11b). In contrast to CsPbI_2Br , $\text{CsPb}_{0.9}\text{Nd}_{0.1}\text{I}_3$ sample exhibited superior stability. UV–Vis measurements show that the absorbance did not decrease

during the first 3 h of measurement. Furthermore, the decrease in absorbance by $\sim 20\%$ and 40% is observed at only 27 and 96 h, respectively. UV–Vis spectra measured at 27 and 96 h show another adsorption edge at 450 nm, in addition to the blue-shifted main one, indicating the transformation of perovskite structure to non-perovskite phase. These results suggest that B-site modulation utilizing Nd doping is more efficient in the stabilization of perovskite structure than X-site modulation by partial replacement of iodine with bromine.

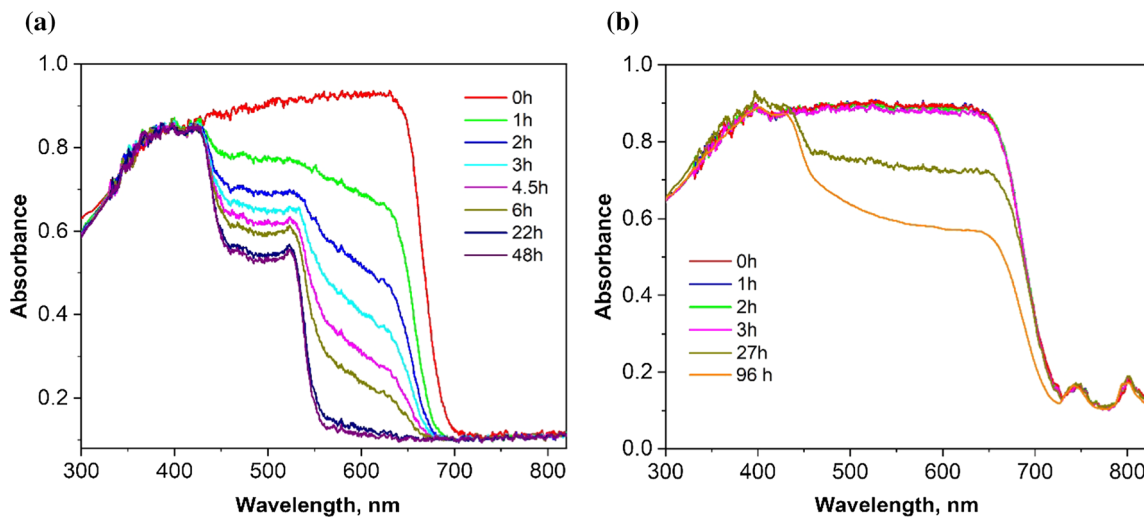


Figure 11 UV–Vis absorption spectra of CsPbI_2Br (a) and $\text{CsPb}_{0.9}\text{Nd}_{0.1}\text{I}_3$ (b) as a function of time.

Discussion

Microstructure observations (Fig. 3) of $\text{CsI} + \text{PbI}_2$ samples allow concluding that during ball milling, ductile PbI_2 particles are plastically deforming to form flattened disks, while brittle CsI particles are primarily fracturing to smaller fragments. Under the dynamic mechanical collisions of balls, fractured CsI fragments penetrate ductile PbI_2 . Flattened disks can also be cold-welded together, resulting in large layered $\text{PbI}_2/\text{CsI}/\text{PbI}_2$ composite particles, where the small CsI fragments appear between PbI_2 layers. The colliding balls further plastically deform the composite particles, resulting in their work hardening. Eventually, composite particles fracture into smaller pieces (Fig. 3) by a fatigue failure mechanism. Such significant changes simultaneously increase the surface area between reactants and produce dislocations that accelerate nucleation of CsPbI_3 particles at the PbI_2/CsI interface.

XRD analysis (Fig. 1) and UV–Vis absorption spectra (Fig. 2) suggest that a significant amount of reactants convert into CsPbI_3 at the very early stages (5 min) of the process. Further conversion of remaining reactants takes a much longer time. For example, the UV–Vis spectra (Fig. 2) of the sample milled for 60 min at cryogenic temperatures still show some traces of reactants. This result proves that CsPbI_3 formed at the CsI/PbI_2 interface creates a barrier between the reactants and significantly slows the synthesis reaction. Extended (30–60 min) milling results in continuous refinements, reduction in

product particle sizes, and creation of fresh contact between reactants, thus facilitating reaction completion.

The milling temperature has a significant influence on the reaction kinetics. The reactants convert to products faster at room temperature (Fig. 2). In general, the temperature of the samples during mechanochemical synthesis can increase due to heating caused by transferring the kinetic energy from the colliding balls and heat released from the reaction itself. We performed DSC analysis of the manually mixed (5 min) $\text{CsI} + \text{PbI}_2$ sample to reveal the possible heat release due to the reaction. This analysis indicates only an endothermic process (Figure S7). We should note that the XRD analysis of manually mixed samples shows no CsPbI_3 before DSC analysis. Therefore, the endothermic process observed on the DSC curve is ascribed to the $\text{CsI} + \text{PbI}_2$ reaction. This result suggests that during milling, the temperature increases only due to the energy transfer from colliding balls.

The milling time has a substantial influence on product particle sizes. The prolonged milling (60–120 min) allows decreasing the particle sizes, but also increases the agglomerate size by the cold welding mechanism (Figs. 4, 5). The use of process-control agents could reduce the cold welding and refine the particle sizes. Indeed, early works [34, 45] show that the use of organic solvents in conjunction with the ball milling allows producing dispersed fine cesium lead halides.

The mechanochemical synthesis mechanisms for $\text{CsI} + \text{PbI}_2$, $\text{CsBr} + \text{PbI}_2$, and $\text{CsBr} + \text{PbBr}_2$ mixtures have many similar aspects. Moreover, DSC curves for $\text{CsI} + \text{PbI}_2$ and $\text{CsBr} + \text{PbI}_2$ exhibit similar endothermic peaks centered at 340 and 325 °C, respectively (Figure S7). We can suggest that those systems can be categorized into a general *brittle-ductile* synthesis type.

The significant differences in product particle size for the $\text{CsPbBr}_3 + 3\text{KI}$ and $\text{CsBr} + \text{PbBr}_2 + 3\text{KI}$ systems (Fig. 7) point to different synthesis mechanisms. $\delta\text{-CsPbI}_3$ produced from the $\text{CsPbBr}_3 + 3\text{KI}$ mixture consists of larger particles similar to CsPbBr_3 reactant (Fig. 5, 60 min). We can suggest that the synthesis of the $\text{CsPbBr}_3 + 3\text{KI}$ mixture can be categorized in the *brittle-brittle* system type. Large particles of KI fracture into many smaller particles first, and then, the halide exchange reaction takes place at the KI/ CsPbBr_3 interface of fine reactant particles. The interaction mechanism of the $\text{CsBr} + \text{PbBr}_2 + 3\text{KI}$ system most likely is similar to the $\text{CsI} + \text{PbI}_2$ case, and the reaction can be classified into the *brittle-ductile* system type.

Adding small amounts of NdI_3 into the $\text{CsI} + \text{PbI}_2$ mixture does not influence the morphological features of the product (Fig. 9). The radius of Nd^{3+} ion (98 pm) is much smaller than that of Pb^{2+} radius (119 pm), and Nd incorporation into the product lattice stabilizes (Figs. 8, 11) perovskite structure due to the increase in the Goldschmidt tolerance factor. DSC curve of the $\text{CsI} + \text{PbI}_2 + \text{NdI}_3$ system exhibits several new endothermic peaks at lower temperatures as compared to the $\text{CsI} + \text{PbI}_2$ mixture (Figure S7). The thermal analysis result (Figure S7) of pure NdI_3 shows a broad endothermic peak presumably related to its melting and/or decomposition processes. We can assume that these processes significantly change the reaction mechanism of the $\text{CsI} + \text{PbI}_2 + \text{NdI}_3$ system. We do not know the extent of localized temperature increase during milling, but we cannot rule out that the local increase in the temperature could trigger the melting of NdI_3 . The presence of the molten phase could accelerate the reaction and facilitate the uniform distribution of the Nd into CsPbI_3 lattice. Future studies should be directed to understand the mechanism of these processes, the chemical states of Nd in the lattice, as well as the origin of superior stability of Nd-doped CsPbI_3 observed in this work.

Conclusions

Microstructure observations reveal the existence of two different product formation mechanisms depending on the mechanical properties of reactants. The synthesis involving mixtures of iodides (CsI , PbI_2 , and KI) and/or bromides (CsBr , PbBr_2) can be categorized into a general *brittle-ductile* mechanism, whereas in the halide exchange reactions, the $\text{CsPbBr}_3 + \text{KI}$ mixture, can proceed via the *brittle-brittle* mechanism. The results reveal that the milling temperature has a significant influence on reaction kinetics. The product particles nucleate and grow at the reactant interface and slow the synthesis reaction by creating a diffusion barrier. Extended milling reduces the product particle sizes and creates fresh contact between reactants, thus facilitating reaction completion. The results suggest that Nd doping is more efficient in the stabilization of the perovskite structure than a partial replacement of iodine with bromine. Future investigations are needed to understand the origin of the superior stability of Nd-doped CsPbI_3 .

Supplementary information

Supplementary Information is available free of charge on the ACS Publications website at DOI: <https://doi.org/10.1007/s10853-020-04617-3>. It contains additional XRD patterns, SEM images, DSC curves, and photographs of samples.

Acknowledgements

The work was performed with financial support in parts from the U.S. Department of Energy (DOE) National Nuclear Security Administration (NNSA, Grant # DE-NA0003888), U.S. National Science Foundation (NSF, PHY-1713857), and JINA-CEE NSF Physics Frontiers Centers (Award #:1430152). A. Aprahamian acknowledges support from the Fulbright U.S. Scholar grant. E. Aleksanyan and K. Manukyan also acknowledge support from Foundation for Armenian Science and Technology (FAST).

Compliance with ethical standards

Conflicts of interest The authors declare no competing financial interest.

Electronic supplementary material: The online version of this article (<https://doi.org/10.1007/s10853-020-04617-3>) contains supplementary material, which is available to authorized users.

References

- [1] Kim HS, Lee CR, Im JH et al (2012) Lead iodide perovskite sensitized all-solid-state submicron thin film mesoscopic solar cell with efficiency exceeding 9%. *Sci Rep* 2:1–7. <https://doi.org/10.1038/srep00591>
- [2] Stoumpos CC, Malliakas CD, Kanatzidis MG (2013) Semiconducting tin and lead iodide perovskites with organic cations: phase transitions, high mobilities, and near-infrared photoluminescent properties. *Inorg Chem* 52:9019–9038. <https://doi.org/10.1021/ic401215x>
- [3] Xiao C, Li Z, Guthrey H et al (2015) Mechanisms of electron-beam-induced damage in perovskite thin films revealed by cathodoluminescence spectroscopy. *J Phys Chem C* 119:26904–26911. <https://doi.org/10.1021/acs.jpcc.5b09698>
- [4] Song J, Li J, Li X et al (2015) Quantum dot light-emitting diodes based on inorganic perovskite cesium lead halides (CsPbX₃). *Adv Mater* 27:7162–7167. <https://doi.org/10.1002/adma.201502567>
- [5] Li Z, Xu J, Zhou S et al (2018) CsBr-induced stable CsPbI_{3-x}Br_x ($x < 1$) perovskite films at low temperature for highly efficient planar heterojunction solar cells. *ACS Appl Mater Interfaces* 10:38183–38192. <https://doi.org/10.1021/acsami.8b11474>
- [6] Wang K, Jin Z, Liang L et al (2018) All-inorganic cesium lead iodide perovskite solar cells with stabilized efficiency beyond 15%. *Nat Commun* 9:1–8. <https://doi.org/10.1038/s41467-018-06915-6>
- [7] Steele JA, Jin H, Dovgaluk I et al (2019) Thermal unequilibrium of strained black CsPbI₃ thin films. *Science* 80(365):679–684. <https://doi.org/10.1126/science.aax3878>
- [8] Zhou Y, Zhao Y (2019) Chemical stability and instability of inorganic halide perovskites. *Energy Environ Sci* 12:1495–1511. <https://doi.org/10.1039/c8ee03559h>
- [9] Wang K, Jin Z, Liang L et al (2019) Chlorine doping for black γ -CsPbI₃ solar cells with stabilized efficiency beyond 16%. *Nano Energy* 58:175–182. <https://doi.org/10.1016/j.nano.2019.01.034>
- [10] Luo P, Xia W, Zhou S et al (2016) Solvent engineering for ambient-air-processed, phase-stable CsPbI₃ in perovskite solar cells. *J Phys Chem Lett* 7:3603–3608. <https://doi.org/10.1021/acs.jpclett.6b01576>
- [11] Frolova LA, Anokhin DV, Piryazev AA et al (2017) Highly efficient all-inorganic planar heterojunction perovskite solar cells produced by thermal coevaporation of CsI and PbI₂. *J Phys Chem Lett* 8:67–72. <https://doi.org/10.1021/acs.jpclett.6b02594>
- [12] Wang Q, Zheng X, Deng Y et al (2017) Stabilizing the α -phase of CsPbI₃ perovskite by sulfobetaine zwitterions in one-step spin-coating films. *Joule* 1:371–382. <https://doi.org/10.1016/j.joule.2017.07.017>
- [13] Wang P, Zhang X, Zhou Y, et al (2018) Solvent-controlled growth of inorganic perovskite films in dry environment for efficient and stable solar cells. *Nat Commun* 9:1–7. <https://doi.org/10.1038/s41467-018-04636-4>
- [14] Dutta A, Pradhan N (2019) Phase-stable red-emitting CsPbI₃ nanocrystals: successes and challenges. *ACS Energy Lett* 4:709–719. <https://doi.org/10.1021/acsenergylett.9b00138>
- [15] Marronnier A, Roma G, Boyer-Richard S et al (2018) Anharmonicity and disorder in the black phases of CsPbI₃ used for stable inorganic perovskite solar cells. *ACS Nano* 12:3477–3486. <https://doi.org/10.1109/PVSC.2018.8547769>
- [16] Sutton RJ, Filip MR, Haghshirad AA et al (2018) Cubic or orthorhombic? Revealing the crystal structure of metastable black-phase CsPbI₃ by theory and experiment. *ACS Energy Lett* 3:1787–1794. <https://doi.org/10.1021/acsenergylett.8b00672>
- [17] Protesescu L, Yakunin S, Bodnarchuk MI et al (2015) Nanocrystals of cesium lead halide perovskites (CsPbX₃, X = Cl, Br, and I): novel optoelectronic materials showing bright emission with wide color gamut. *Nano Lett* 15:3692–3696. <https://doi.org/10.1021/nl5048779>
- [18] Travis W, Glover ENK, Bronstein H et al (2016) On the application of the tolerance factor to inorganic and hybrid halide perovskites: a revised system. *Chem Sci* 7:4548–4556. <https://doi.org/10.1039/c5sc04845a>
- [19] Li Z, Yang M, Park JS et al (2016) Stabilizing perovskite structures by tuning tolerance factor: formation of formamidinium and cesium lead iodide solid-state alloys. *Chem Mater* 28:284–292. <https://doi.org/10.1021/acs.chemmater.5b04107>
- [20] Akkerman QA, Meggiolaro D, Dang Z et al (2017) Fluorescent alloy CsPb_xMn_{1-x}I₃ perovskite nanocrystals with high structural and optical stability. *ACS Energy Lett* 2:2183–2186. <https://doi.org/10.1021/acsenergylett.7b00707>
- [21] Zou S, Liu Y, Li J et al (2017) Stabilizing cesium lead halide perovskite lattice through Mn(II) substitution for air-stable light-emitting diodes. *J Am Chem Soc* 139:11443–11450. <https://doi.org/10.1021/jacs.7b04000>
- [22] Liu F, Ding C, Zhang Y et al (2017) Colloidal synthesis of air-stable alloyed CsSn_{1-x}Pb_xI₃ perovskite nanocrystals for use in solar cells. *J Am Chem Soc* 139:16708–16719. <https://doi.org/10.1021/jacs.7b08628>

[23] Yao JS, Ge J, Wang KH et al (2019) Few-nanometer-sized α -CsPbI₃ Quantum Dots Enabled by Strontium Substitution and Iodide Passivation for Efficient Red-Light Emitting Diodes. *J Am Chem Soc* 141:2069–2079. <https://doi.org/10.1021/jacs.8b11447>

[24] Hu Y, Bai F, Liu X et al (2017) Bismuth incorporation stabilized α -CsPbI₃ for fully inorganic perovskite solar cells. *ACS Energy Lett* 2:2219–2227. <https://doi.org/10.1021/acsenergylett.7b00508>

[25] Xiang S, Li W, Wei Y et al (2018) The synergistic effect of non-stoichiometry and Sb-doping on air-stable α -CsPbI₃ for efficient carbon-based perovskite solar cells. *Nanoscale* 10:9996–10004. <https://doi.org/10.1039/c7nr09657g>

[26] Jena AK, Kulkarni A, Sanehira Y et al (2018) Stabilization of α -CsPbI₃ in ambient room temperature conditions by incorporating Eu into CsPbI₃. *Chem Mater* 30:6668–6674. <https://doi.org/10.1021/acs.chemmater.8b01808>

[27] Dastidar S, Egger DA, Tan LZ et al (2016) High Chloride Doping Levels Stabilize the Perovskite Phase of Cesium Lead Iodide. *Nano Lett* 16:3563–3570. <https://doi.org/10.1021/acs.nanolett.6b00635>

[28] Jing Q, Zhang M, Huang X et al (2017) Surface passivation of mixed-halide perovskite CsPb(Br:XI_{1-x})₃ nanocrystals by selective etching for improved stability. *Nanoscale* 9:7391–7396. <https://doi.org/10.1039/c7nr01287j>

[29] He Y, Gong J, Zhu Y et al (2018) Highly pure yellow light emission of perovskite CsPb(BrxI_{1-x})₃ quantum dots and their application for yellow light-emitting diodes. *Opt Mater (Amst)* 80:1–6. <https://doi.org/10.1016/j.optmat.2018.04.009>

[30] Manukyan KV, Yeghishyan AV, Moskovskikh DO et al (2016) Mechanochemical synthesis of methylammonium lead iodide perovskite. *J Mater Sci* 51:9123–9130. <https://doi.org/10.1007/s10853-016-0165-4>

[31] Karmakar A, Askar AM, Bernard GM et al (2018) Mechanochemical synthesis of methylammonium lead mixed-halide perovskites: unraveling the solid-solution behavior using solid-state NMR. *Chem Mater* 30:2309–2321. <https://doi.org/10.1021/acs.chemmater.7b05209>

[32] Sarkar A, Acharyya P, Sasmal R et al (2018) Synthesis of ultrathin few-layer 2D nanoplates of halide perovskite Cs₃Bi₂I₉ and single-nanoplate super-resolved fluorescence microscopy. *Inorg Chem* 57:15558–15565. <https://doi.org/10.1021/acs.inorgchem.8b02887>

[33] Jodlowski AD, Yépez A, Luque R et al (2016) Benign-by-design solventless mechanochemical synthesis of three-, two-, and one-dimensional hybrid perovskites. *Angew Chem Int Ed* 55:14972–14977. <https://doi.org/10.1002/anie.201607397>

[34] Palazon F, El Ajouri Y, Bolink HJ (2019) Making by grinding: mechanochemistry boosts the development of halide perovskites and other multinary metal halides. *Adv Energy Mater* 1902499:1902499. <https://doi.org/10.1002/aem.201902499>

[35] Elseman AM, Shalan AE, Rashad MM, Hassan AM (2017) Experimental and simulation study for impact of different halides on the performance of planar perovskite solar cells. *Mater Sci Semicond Process* 66:176–185. <https://doi.org/10.1016/j.mssp.2017.04.022>

[36] Pal P, Saha S, Banik A et al (2018) All-solid-state mechanochemical synthesis and post-synthetic transformation of inorganic perovskite-type halides. *Chem A Eur J* 24:1811–1815. <https://doi.org/10.1002/chem.201705682>

[37] Singhal N, Chakraborty R, Ghosh P, Nag A (2018) Low-bandgap Cs₄CuSb₂Cl₁₂ layered double perovskite: synthesis, reversible thermal changes, and magnetic interaction. *Chem Asian J* 13:2085–2092. <https://doi.org/10.1002/asia.201800635>

[38] El Ajouri Y, Chirvony VS, Sessolo M et al (2018) Incorporation of potassium halides in the mechanosynthesis of inorganic perovskites: feasibility and limitations of ion-replacement and trap passivation. *RSC Adv* 8:41548–41551. <https://doi.org/10.1039/c8ra08823c>

[39] Jiang G, Guhrenz C, Kirch A et al (2019) Highly luminescent and water-resistant CsPbBr₃-CsPb₂Br₅ perovskite nanocrystals coordinated with partially hydrolyzed poly(methyl methacrylate) and polyethylenimine. *ACS Nano* 13:10386–10396. <https://doi.org/10.1021/acsnano.9b04179>

[40] Karmakar A, Dodd MS, Zhang X et al (2019) Mechanochemical synthesis of 0D and 3D cesium lead mixed halide perovskites. *Chem Commun* 55:5079–5082. <https://doi.org/10.1039/c8cc09622h>

[41] García-Espejo G, Rodríguez-Padrón D, Luque R et al (2019) Mechanochemical synthesis of three double perovskites: Cs₂AgBiBr₆, (CH₃NH₃)₂TlBiBr₆ and Cs₂AgSbBr₆. *Nanoscale* 11:16650–16657. <https://doi.org/10.1039/c9nr06092h>

[42] Sasaki M, Prochowicz D, Marynowski W, Lewiński J (2019) Mechanosynthesis, optical, and morphological properties of MA, FA, Cs-SnX₃ (X = I, Br) and phase-pure mixed-halide MASn_xBr_{3-x} perovskites. *Eur J Inorg Chem* 2019:2680–2684. <https://doi.org/10.1002/ejic.201801506>

[43] Martínez-Sarti L, Palazon F, Sessolo M, Bolink HJ (2020) Dry mechanochemical synthesis of highly luminescent, blue and green hybrid perovskite solids. *Adv Opt Mater* 8:2–8. <https://doi.org/10.1002/adom.201901494>

[44] Rosales BA, Wei L, Vela J (2019) Synthesis and mixing of complex halide perovskites by solvent-free solid-state

methods. *J Solid State Chem* 271:206–215. <https://doi.org/10.1016/j.jssc.2018.12.054>

[45] Chen D, Li J, Chen X et al (2019) Grinding synthesis of APbX_3 ($\text{A} = \text{MA, FA, Cs}$; $\text{X} = \text{Cl, Br, I}$) perovskite nanocrystals. *ACS Appl Mater Interfaces* 11:10059–10067. <https://doi.org/10.1021/acsami.8b19002>

[46] Protesescu L, Yakunin S, Nazarenko O et al (2018) Low-cost synthesis of highly luminescent colloidal lead halide perovskite nanocrystals by wet ball milling. *ACS Appl Nano Mater* 1:1300–1308. <https://doi.org/10.1021/acsanm.8b00038>

[47] Kubicki DJ, Prochowicz D, Pinon A et al (2019) Doping and phase segregation in Mn_2 -and Co_{2+} -doped lead halide perovskites from ^{133}Cs and ^{1}H NMR relaxation enhancement. *J Mater Chem A* 7:2326–2333. <https://doi.org/10.1039/c8ta11457a>

[48] Xiang W, Wang Z, Kubicki DJ et al (2019) Europium-Doped CsPbI_2Br for Stable and Highly Efficient Inorganic Perovskite Solar Cells. *Joule* 3:205–214. <https://doi.org/10.1016/j.joule.2018.10.008>

[49] Crane MJ, Kroupa DM, Roh JY et al (2019) Single-source vapor deposition of quantum-cutting $\text{Yb}^{3+}:\text{CsPb}(\text{Cl}_{1-x}\text{Br}_x)_3$ and other complex metal-halide perovskites. *ACS Appl Energy Mater* 2:4560–4565. <https://doi.org/10.1021/acsam.9b00910>

[50] Zhu ZY, Yang QQ, Gao LF et al (2017) Solvent-free mechanosynthesis of composition-tunable cesium lead halide perovskite quantum dots. *J Phys Chem Lett* 8:1610–1614. <https://doi.org/10.1021/acs.jpclett.7b00431>

[51] Hong Z, Tan D, John RA et al (2019) Completely solvent-free protocols to access phase-pure, metastable metal halide perovskites and functional photodetectors from the precursor salts. *iScience* 16:312–325. <https://doi.org/10.1016/j.isci.2019.05.042>

[52] Leupold N, Schötz K, Cacovich S et al (2019) High versatility and stability of mechanochemically synthesized halide perovskite powders for optoelectronic devices. *ACS Appl Mater Interfaces* 11:30259–30268. <https://doi.org/10.1021/acsm.9b09160>

[53] Palazon F, El Ajouri Y, Sebastia-Luna P et al (2019) Mechanochemical synthesis of inorganic halide perovskites: evolution of phase-purity, morphology, and photoluminescence. *J Mater Chem C* 7:11406–11410. <https://doi.org/10.1039/c9tc03778k>

[54] Bella F, Renzi P, Cavallo C, Gerbaldi C (2018) Caesium for perovskite solar cells: an overview. *Chem Eur J* 24:12183–12205. <https://doi.org/10.1002/chem.201801096>

[55] Manukyan KV, Mason BA, Groven LJ et al (2012) Tailored reactivity of $\text{Ni} + \text{Al}$ nanocomposites: microstructural correlations. *J Phys Chem C* 116:21027–21038. <https://doi.org/10.1021/jp303407e>

[56] Manukyan KV, Lin YC, Rouvimov S et al (2013) Microstructure-reactivity relationship of $\text{Ti} + \text{C}$ reactive nanomaterials. *J Appl Phys* 113:024302. <https://doi.org/10.1063/1.4773475>

Publisher's Note Springer Nature remains neutral with regard to jurisdictional claims in published maps and institutional affiliations.